Spray-Deposited TiO$_2$ Layers on Aluminum Foil for Sustainable Water Remediation

Sanja J. Armaković [1,2], Maria M. Savanović [1,2,*] and Stevan Armaković [2,3]

1 Department of Chemistry, Biochemistry and Environmental Protection, Faculty of Sciences, University of Novi Sad, 21000 Novi Sad, Serbia; sanja.armakovic@dh.uns.ac.rs
2 Association for the International Development of Academic and Scientific Collaboration (AIDASCO), 21000 Novi Sad, Serbia
3 Department of Physics, Faculty of Sciences, University of Novi Sad, 21000 Novi Sad, Serbia; stevan.armakovic@df.uns.ac.rs
* Correspondence: maria.savanovic@dh.uns.ac.rs

Abstract: In this study, we developed TiO$_2$-coated aluminum (TiO$_2$/Al) surfaces using eco-friendly methods to create efficient and environmentally friendly photoactive materials with the potential to enhance water purification systems. TiO$_2$ particles were deposited onto aluminum foil surfaces via a spray method, followed by heat treatment at 200 °C for 15 min. The morphology of the TiO$_2$/Al surfaces, both before and after photocatalytic treatment, was characterized using scanning electron microscopy (SEM) and energy-dispersive X-ray spectroscopy (EDS). The photocatalytic properties of these modified surfaces were evaluated through the degradation of rhodamine B (RB), methylene blue (MB), and methyl orange (MO) under simulated solar and UV–LED irradiation. Among the dyes tested, MO exhibited the highest degradation, influenced by factors such as absorption maximum, molecular structure, charge, and the number of condensed rings. The computational study of interactions between dye molecules and the combined nanoparticle revealed that the binding was the strongest in the case of MO dye. This study also explored the influence of varying the number of TiO$_2$/Al surfaces in solution (one, five, and ten) on the photodegradation efficiency. The solution with five TiO$_2$/Al surfaces demonstrated optimal performance, achieving a 16% degradation of RB. The reusability of the TiO$_2$/Al surfaces was confirmed through five successive runs of RB degradation. The results indicate that TiO$_2$/Al surfaces are a promising solution for addressing water contamination challenges and advancing sustainable water treatment practices.

Keywords: TiO$_2$ coatings; dyes; characterization studies; photocatalysis; nanomaterials; water purification; computational study

1. Introduction

The textile industry is a major polluting agent. Wastewater is generated during the various dyeing and finishing processes of textiles [1]. This wastewater usually contains large amounts of harmful substances, such as dyes, which need treatment before being discharged into the environment [2]. There are more than 100,000 commercially available dyes, with over 7×10^5 tons of synthetic dye being produced annually in the world [3]. The synthetic dyes used in textiles (clothes, fabric), plastic, leather, paper, pharmaceutical, food, color photography, and cosmetic industries are often non-biodegradable, difficult to degrade, and harmful to the environment [4–6]. Dyes are stable in both sunlight and water, and sewage containing dyes can affect aquatic life as well as the flora and fauna surrounding the location of their disposal [7]. The release of dyes in natural waters can interfere with the light required for photosynthesis and can reduce light penetration [8]. When they are excited to higher electronic states, dyes in a specific range can produce singlet oxygen, a toxic substance that can damage aquatic ecosystems and affect the functions of aquatic organisms. In addition, the release of dyes can have toxic effects at low concentrations and

can lead to mutagenic and carcinogenic changes in the environment [9,10]. In the field of medicine, dyes can lead to human skin, eye, and mucous membrane diseases and can even cause tumors [11,12].

Photocatalysis is a technology that utilizes the photoexcitation of semiconductors to promote redox reactions on their surfaces, oxidizing organic substances [13] and reducing specific inorganic substances (e.g., O_2, CO_2, NO_3^-, Fe^{3+}, $Cr_2O_7^{2-}$, and Ag^+) into species that are either stable at the semiconductor surface or easy to remove by external means [14]. The activity range of the photocatalytic process is then defined by the energy required to promote electrons from the valence band to the conduction band of the semiconductor [15]. In that regard, the process is mainly restricted to UV-semiconductors, such as TiO_2 [16], ZnO [17], Bi_2WO_6 [18], WO_3 [19], etc.

Although the photocatalysis process is reaching a degree of technological maturity, a significant disadvantage has been the expensive nature of the relatively pure semiconductor obtaining adequate performance [20]. For example, TiO_2 (anatase) with a 50 nm diameter absorbs only ca. 2% of the Sun's energy [21]. Various approaches have been developed to extend the range of photoactivation of TiO_2 or narrow-band gap semiconductors [22]. The approaches utilized clusters of metal nanoparticles at the surface of the semiconductor [23], acting as light-gatherers, i.e., an antenna system [21]. More successfully, the semiconductor is sensitized by adsorbed porphyrins [24] or block polymer assemblies, which can absorb a significant portion of the visible portion of the solar spectrum [25]. Also, the problem is removing the photocatalyst from the suspension, which increases photocatalytic process costs. This can be improved by using nanomaterials as coatings [26,27].

TiO_2 is now in the limelight due to its outstanding material properties, which are now being exploited for numerous applications [21]. Its flexibility during application and use, as well as its properties, make TiO_2 a very popular additive as product designers and researchers around the world look to use its UV-protective functions in a range of industries [28]. One of the significant applications of TiO_2 is to protect surfaces such as polymers, paintings, and textiles [29]. TiO_2 has an excellent ability to absorb UV radiation due to its high extinction coefficient and is chemically inert, transparent, and stable beyond its phase transition temperature [30]. When using TiO_2 particles, the transparent properties of the coating are limited by the volume fraction of the particles in the coating since particles inside the coating reduce the transparency of the material [31]. Another option is the use of thin TiO_2 films. These coatings can provide UV protection with high visible light transmission. Such coatings are attractive for transparent color coatings on polymers for use in automobile and aerospace applications. In particular, clear coatings have been commercialized for visible and UV protection applications based on a TiO_2/SiO_2 layer system [32]. The sol–gel coating process is widely used for manufacturing such films. In general, these films are durable and provide moderate UV absorption derived from their refractive index [33]. TiO_2 coatings are often used in photocatalysis since they can offer high photocatalytic activity with UV activation of TiO_2, with the possibility of reusing them multiple times. The ability to control the composition of the solution, applied film thickness, and processing parameters, such as heat treatment, makes this technique ideal for tuning film properties for specific applications [34–36].

This study aims to efficiently produce and characterize TiO_2-coated aluminum (TiO_2/Al) photoactive surfaces using eco-friendly methods for potential applications in sustainable water purification. The TiO_2 layer films were deposited onto aluminum foil using a spray method, followed by heat treatment at 200 °C for 15 min. The morphology of the modified surfaces was analyzed using scanning electron microscopy (SEM) and energy-dispersive X-ray spectroscopy (EDS) both before and after photocatalytic treatment.

SEM/EDS analysis revealed that spherical TiO_2 particles were well deposited into the tunnel-like morphology of the aluminum foil. This study further investigated the photocatalytic activity of these surfaces through the degradation of rhodamine B (RB), methylene blue (MB), and methyl orange (MO) under simulated solar (SS) and UV–LED irradiation. The optimal number of TiO_2/Al layers for effective RB photodegradation was

determined to be five, achieving a 16% degradation rate. Additionally, the reusability of the TiO_2/Al surfaces was assessed through five successive runs of RB degradation, demonstrating their potential for sustainable water purification. Within different dyes studied, MO exhibited the highest degradation, influenced by factors such as absorption maximum, molecular structure, charge, and the number of condensed rings, additionally confirmed by computational analysis.

These findings highlight the potential of the modified TiO_2/Al layer surfaces as a promising solution for addressing water contamination challenges and advancing eco-friendly wastewater treatment methods.

2. Materials and Methods

2.1. Chemicals and Solutions

All used chemicals were of reagent grade and were used without further purification. Chemicals used were RB ($C_{28}H_{31}ClN_2O_3$, >99.9%, Merck, Darmstadt, Germany), MB ($C_{16}H_{18}ClN_3S$, >99%, Merck, Darmstadt, Germany), MO ($C_{14}H_{14}N_3NaO_3S$, >99.9%, Kemika, Zagreb, Croatia), ethanol (C_2H_6O, >99.8%, Merck, Darmstadt, Germany), and TiO_2 Hombikat (100% anatase, Sigma-Aldrich, Darmstadt, Germany, specific surface area 35–65 m^2/g). $K_2Cr_2O_7$ (Kemika, Zagreb, Croatia), H_2SO_4 (95–97%, Pharma Hemija, Šabac, Serbia), $HgSO_4$ ($\geq$99.6%, Lach-Ner, Neratovice, Czech Republic), and Ag_2SO_4 ($\geq$99.9%, Sigma–Aldrich, Darmstadt, Germany) were used for Chemical Oxygen Demand (COD) determination. The dye solutions were made using ultrapure water (κ = 0.055 $\mu S/cm$, pH 6.56, total organic carbon TOC < LOD). The dye stock solution concentration was 0.05 $mmol/dm^3$. For the deposition, commercial household aluminum foil was used. The thickness of the aluminum foil was 0.05 mm, according to the producer's specification.

2.2. Synthesis of Samples

The cold spray, a relatively new technology, was used to prepare aluminum surfaces coated with TiO_2 in the form of tiles. Namely, TiO_2/Al surfaces were prepared using the homogeneous solution of 1.0 mg/cm^3 TiO_2. The prepared and sonicated TiO_2 solution was sprayed on an Al foil surface three times on each side of the foil, making layers of TiO_2 on foil surfaces. Then, foils were annealed at 200 °C for 15 min. Produced foils were 10 mm × 10 mm, surface 100 mm^2, and foil thickness of 0.05 mm.

2.3. Characterization Methods

The structure of TiO_2/Al surfaces is assessed using SEM. The presence of TiO_2 particles on Al foil was detected using a JEOL JSM-6460LV operating at 20 keV. SEM analysis was conducted, utilizing an EDS detector, explicitly using the INCAx-sight detector and 'INAx-stream' pulse processor from Oxford Instruments, to ascertain the composition and quality of TiO_2/Al surfaces.

2.4. Photodegradation Experiments

Direct photolysis and photocatalysis experiments, under the influence of SS and UV–LED irradiation, were carried out in a double-layer heat-resistant glass-jacketed beaker photocatalytic reactor (total volume of ca. 50 cm^3, liquid layer thickness 10 mm), with a top opening on which the radiation beam was focused. The cell was equipped with a magnetic stir bar and a water-circulating jacket, and the solutions were continuously stirred during the photodegradation process. Before photodegradation experiments, the effect of the diffusion of dyes was preliminarily checked. The diffusion did not affect photodegradation experiments. The dye solution was thermostated at (25 $\pm$ 0.5) °C for 5 min and then irradiated. The mixture was stirred at a constant rate during irradiation. Experiments were performed using 10 cm^3 of 0.05 $mmol/dm^3$ RB, MB, and MO and irradiated for 300 min. All experiments of direct photolysis and photodegradation were performed at natural pH in order to simulate natural conditions and reduce process costs. The number of used TiO_2/Al surfaces in the reaction mixture was one, five, and ten. The SS irradiation source was a 50 W

halogen lamp (Philips, Amsterdam, The Netherlands, with an intensity of 661.0 W/m^2 in the visible region and 1.071 W/m^2 in the UV region). The UV–LED radiation source was a 5 W UV–LED Lamp (Enjoydeal, Hong Kong, China, type: MR16 AC 85-265V/12, with an intensity of 107.2 W/m^2 in the visible and 14.356 W/m^2 in the UV region).

2.5. Analytical Procedures

At the beginning of the experiment and at regular time intervals, aliquots of 1.00 cm^3 were taken from the reaction mixture, and its absorbance was measured using a spectrophotometric technique. After the measurements, the samples were returned to the reaction mixture so that sampling did not cause a volume variation, and the degradation procedure was continued. The adsorption of dye molecules on TiO$_2$/Al surfaces was preliminarily checked, and none of the used dye molecules was adsorbed on the TiO$_2$/Al surfaces.

2.5.1. Spectrophotometric Measurements

Absorbance was recorded on a double-beam T80+UV/Vis Spectrometer (PG Instruments, Wibtoft, UK) at the fixed slit width (2 nm) using a quartz cell (1 cm optical length) and computer-loaded UV Win 5 data software (version 5.0). The evolution of absorbance of the dye solution was recorded at 660 nm for MB, 560 nm for RB, and 460 nm for MO (Figure 1). The degradation efficiency is determined as A/A_0, wherein A represents the absorbance of the dye solution measured in the chosen time intervals, and A_0 represents the absorbance of the initial dye solution before the degradation process. Therefore, A/A_0 represents the concentration of the dye present in the solution at the chosen interval point.
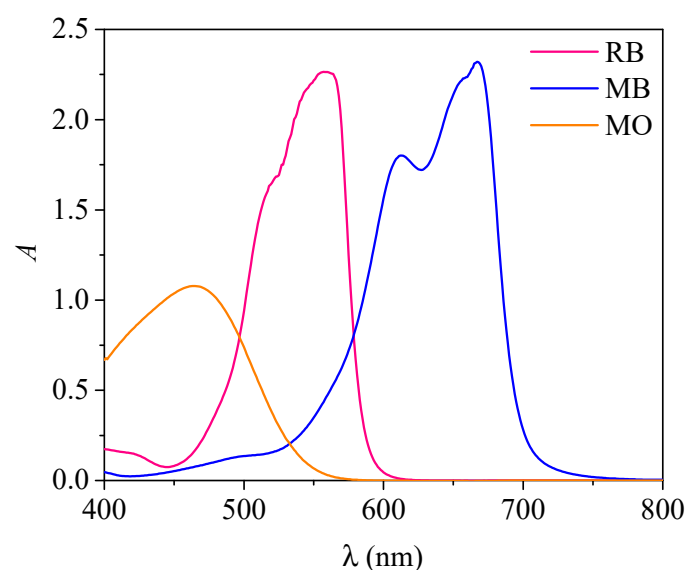

Figure 1. Absorption spectra of selected dyes.

2.5.2. COD Measurements

COD was determined according to Standard Method 410.4, which the EPA United States Environmental Protection Agency declared. Aliquots of 2.5 cm^3 were taken from the reaction mixture after 300 min of photodegradation experiments. The COD concentration was determined photometrically by measuring the absorbance of the formed Cr^{3+}. The evolution of the absorbance of the digested solution was recorded at 600 nm. The samples were digested at 150 °C for 2 h.

2.5.3. Emission Spectra Measurements

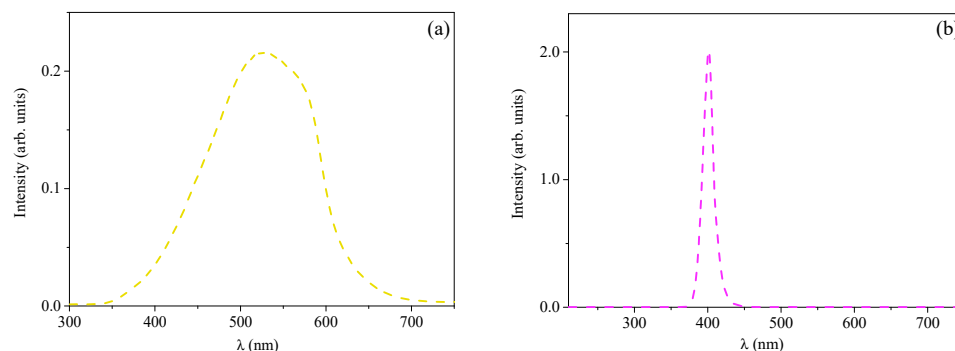The emission spectra of both lamps (Figure 2) used were recorded on an Ocean Optics Spectrometer.

Figure 2. Emission spectra of the (**a**) 50 W halogen lamp and (**b**) 5 W UV–LED lamp.

2.5.4. Energy Flux Measurements

The UV energy fluxes were measured using a Delta Ohm HD 2102.2 (Padova, Italy). The radiometer was fitted with the LP 471 UVA sensor (spectral range 315–400 nm) for measuring UV energy, and in the case of Vis energy, the radiometer was fitted with the LP 471 RAD (spectral range 400–1050 nm).

2.6. Computational Details

The computational study in this work encompassed several quantum mechanical levels of theory. Dye molecules were pre-optimized using the GFN2-xTB method, developed by Prof. Grimme and coworkers [37–41], and re-optimized using PBE [42] functional with D3 correction [43–45] and 6–31G(d,p) basis set. Nanoparticle structures and the resulting complex were geometrically optimized using the PBE-D3 level of theory with the def2-SV(P) basis set, followed by single point energy calculations with the ωB97X-3c [46] method in order to calculate binding energies. The same approach was applied in the investigation of the interaction between dye molecules and nanoparticles resulting from the interaction between Al and TiO_2 clusters. Binding energies between nanostructures and dyes and the resulting nanostructure were calculated according to the following equations:

$$E_b = E_{tot}(Al + TiO_2) - E(Al) - E(TiO_2) \tag{1}$$

$$E_b = E_{tot}(AlTiO_2 + dye) - E(AlTiO_2) - E(dye) \tag{2}$$

where in Equation (1) $E_{tot}(Al + TiO_2)$ denotes the total energy of the optimized complex consisting of Al and TiO_2 nanoparticles; $E(Al)$ denotes the total energy of the optimized Al nanoparticle; and $E(TiO_2)$ denotes the total energy of a TiO_2 nanoparticle. Furthermore, in Equation (2), $E_{tot}(AlTiO_2 + dye)$ denotes the total energy of the optimized complex consisting of $AlTiO_2$ and dye molecule; $E(AlTiO_2)$ denotes the total energy of the optimized $AlTiO_2$ nanoparticle; and $E(dye)$ denotes the total energy of a dye molecule. Initial Al nanostructure was generated using the nanoparticle builder of the Schrödinger Materials Science Suite 2022-2 (SMSS) [47–50], while the initial structure of TiO_2 nanoparticle was taken from the reference [51] (precisely, the ground state geometry of TiO_2 nanocluster with five TiO_2 units).

DFT calculations were performed using the ORCA6 [52–60] molecular modeling package. GFN2-xTB calculations were performed as implemented in the xtb 6.7.0. program. GFN2-xTB calculations were run within the atomistica.online molecular modeling platform [61,62], freely available at https://atomistica.online (accessed on 1 July 2024).

3. Results and Discussion

3.1. SEM and EDS Measurements

The SEM is a powerful technique that utilizes electron beam interactions with materials to generate a wide range of data on various material types [63]. Therefore, the SEM technique was applied to obtain insights into the particle characterization and surface

morphology of the examined samples. An elemental microanalysis with SEM/EDS provided insight into the control samples of TiO_2 and Al foil. It indicated mainly spherical particles of TiO_2 and a grooved or textured morphology of the Al foil (Figure 3). Table 1 provides the chemical composition from EDS spectra, and as can be seen, the TiO_2 and Al foil did not have impurities present. SEM micrographs of the prepared TiO_2/Al surfaces revealed spherical TiO_2 particles deposited within the grooves or surface features of the Al foil. The deposition of TiO_2 on the Al foil resulted in a TiO_2/Al composite, with TiO_2 particles observed within the textured surface of the Al foil. The TiO_2 particles appear to be arranged with consistent spacing, which could facilitate interaction between dye molecules, TiO_2, and the Al surface during the degradation process (Figure 3). SEM micrographs also indicate that the TiO_2/Al surfaces exhibit a relatively inhomogeneous distribution of TiO_2 particles. Additionally, the TiO_2/Al surfaces are characterized by a dense network of TiO_2 particles. This distribution of TiO_2 on the Al foil surface suggests that the deposition may influence the material's photocatalytic performance.
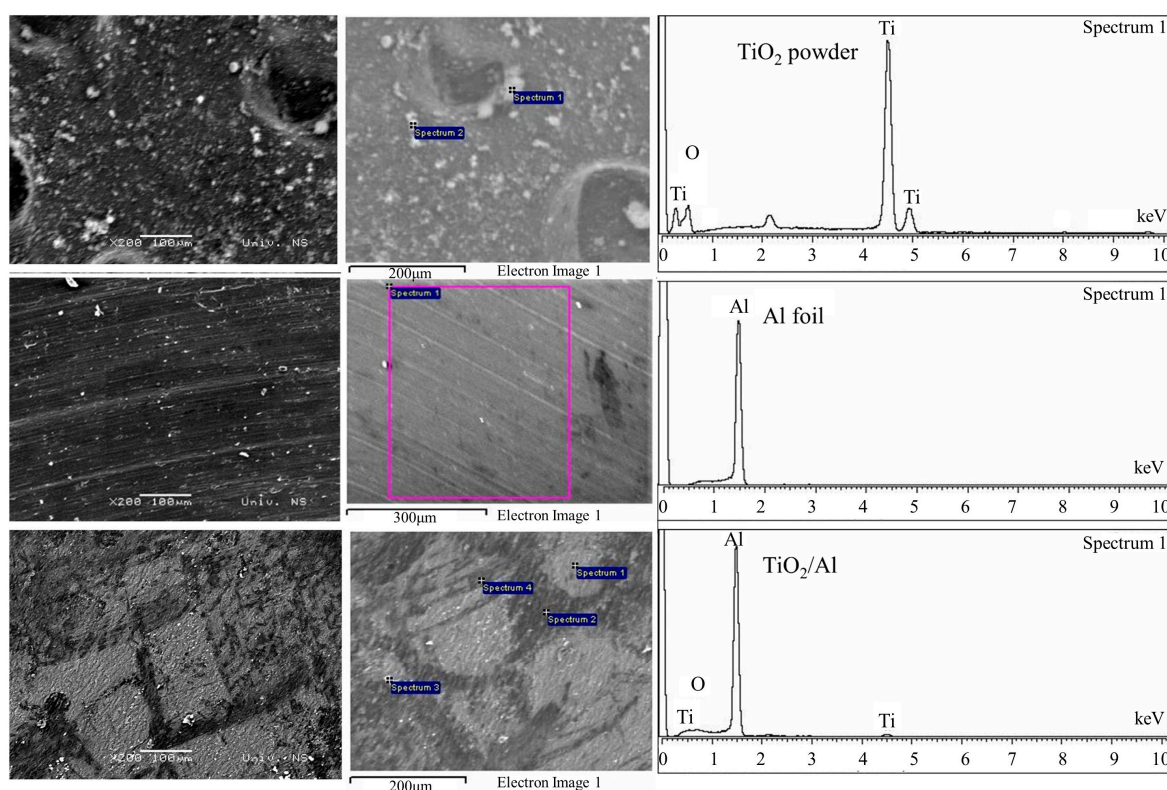

Figure 3. The SEM micrographs and EDS spectra of TiO_2, Al, and modified TiO_2/Al surfaces.

Table 1. EDS results for TiO_2, Al, and modified TiO_2/Al surfaces.

Sample	EDS Results			
	O (wt%)	Ti (wt%)	Al (wt%)	Total (wt%)
TiO_2	33.81	66.19	–	100.00
Al	–	–	100.00	100.00
TiO_2/Al	10.79	2.96	86.25	100.00
TiO_2/Al after one treatment	9.54	3.20	87.26	100.00
TiO_2/Al after five treatments	9.62	2.77	87.61	100.00

Further, used TiO_2/Al surfaces were studied by SEM/EDS after one and five photocatalytic treatments to provide insight into the coating's reusability. As can be seen from Figures 4 and 5, both SEM micrographs and digital photos of synthesized TiO_2/Al surfaces after one and five photocatalytic treatments look very similar. Also, the wt% content of Ti and O remains consistent across all TiO_2/Al samples (Table 1), suggesting a proportional distribution of TiO_2 within the samples and effective deposition on the Al foil surface.
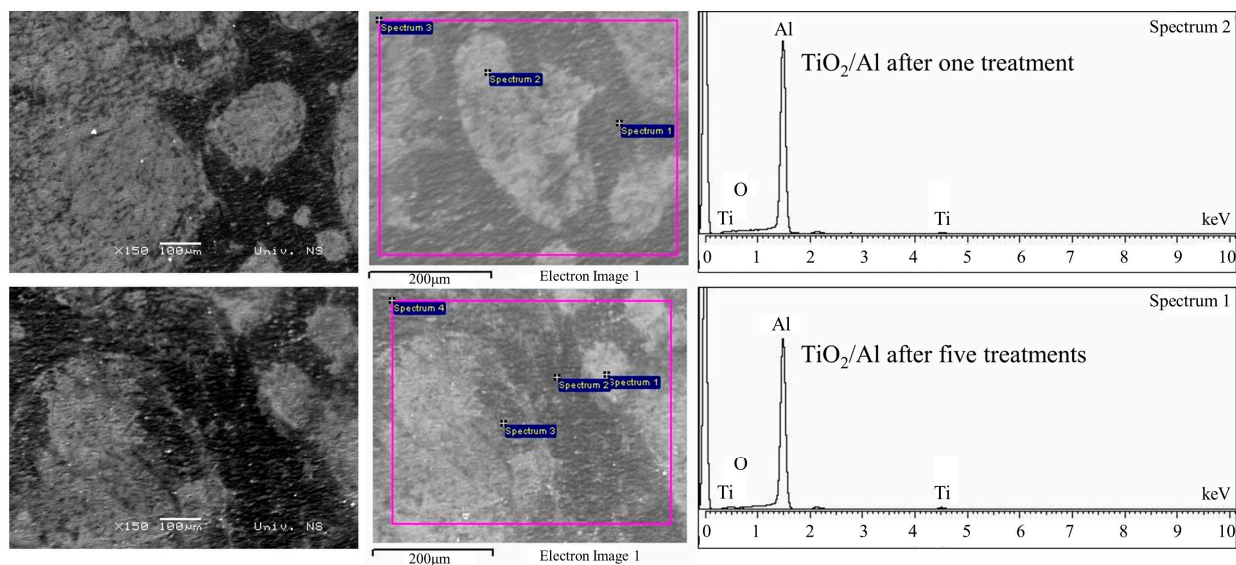
Figure 4. The SEM micrographs and EDS spectra of modified TiO_2/Al surfaces after one and five treatments of photodegradation.
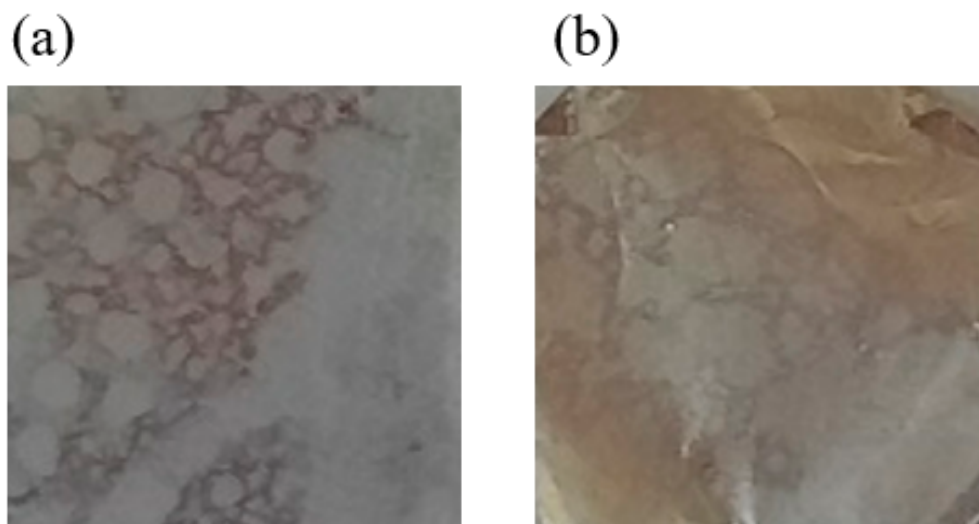

Figure 5. Digital photos of synthesized TiO_2/Al surfaces (**a**) before and (**b**) after photodegradation.

The fundamental observation of the TiO_2/Al surface after photodegradation treatment is that TiO_2 particles remained stably present on the Al surface. SEM micrographs (Figure 4) and EDS measurements (Table 1) confirm that TiO_2 particles were well-distributed within the textured surface of the Al foil and remained in place even after five photodegradation treatments. This indicates that the prepared surfaces have maintained their integrity, fulfilling the primary objective of their preparation. Namely, after the treatment of photodegradation, when the catalyst is dispersed in the solution, there is a need for the removal of the catalyst, which requires time and can increase and affect the cost of the entire process significantly. However, when TiO_2 nanoparticles are attached to the surfaces as TiO_2/Al surfaces, they can be easily removed from the solution after the photodegradation process,

washed, dried, and then reused. Also, the low processing cost and synthesis at low temperatures favor TiO_2/Al surfaces. Overall, the TiO_2/Al surfaces were stable and had good properties closely related to their microstructure.

3.2. Photocatalytic Degradation of RB and Surface Reusability

RB was not degraded during direct photolysis or by using pure Al foil under UV-LED irradiation. Therefore, the deposition of oxidants such as TiO_2 on Al surfaces resulted in quenching of conduction band electrons and generation of reactive $\bullet OH$ radicals, enhancing the decolorization of dyes in the presence of UV–LED irradiation.

First, the efficiency of photocatalytic degradation of RB using different numbers of TiO_2/Al surfaces under UV–LED irradiation was examined (Figure 6a). In our experiments, we considered different numbers of plates per constant volume. By keeping the reactor volume constant, we ensured that the observed differences in efficiency were solely due to the variation in surface area and not influenced by changes in mass transfer or reactor conditions. During the photodegradation process, one TiO_2/Al (1-TiO_2/Al), five TiO_2/Al (5-TiO_2/Al), or ten TiO_2/Al (10-TiO_2/Al)/produced tiles/surfaces were used in photodegradation of RB. During the photocatalytic degradation of RB using 1-TiO_2/Al, the degradation efficiency was 3% after 300 min of irradiation. With the increase in the number of used surfaces, the efficiency of degradation also increased. When using 5-TiO_2/Al surfaces, the degradation efficiency was 16%, while when using 10-TiO_2/Al surfaces, the degradation efficiency was 24%. These results imply that the optimal degradation of dye was achieved using 5-TiO_2/Al surfaces, since with the increasing number of used surfaces on five, degradation efficiency increased by 13%. Also, COD measurements were performed, which gave insight into the mineralization of RB. During direct photolysis and by using 1-TiO_2/Al, mineralization was not observed. With the use of 5-TiO_2/Al and 10-TiO_2/Al, mineralization efficiency increased, and it was 5% and 6%, respectively.
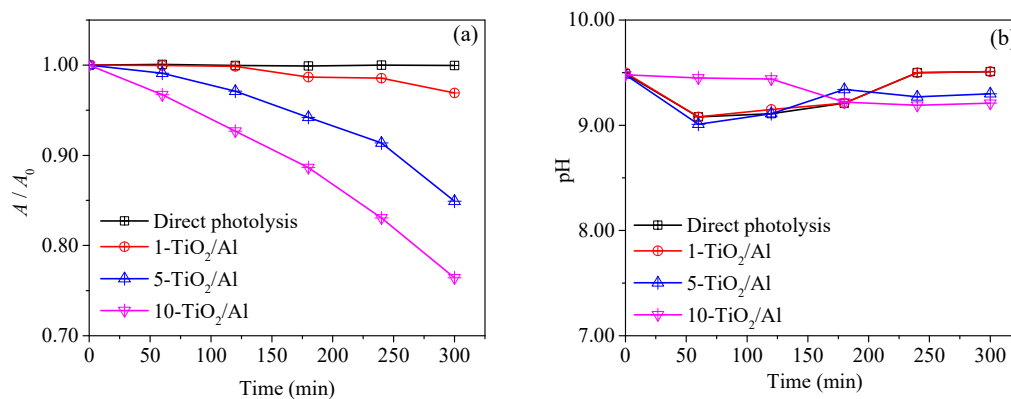

Figure 6. (**a**) The efficiency of photocatalytic degradation of RB using different numbers of TiO_2/Al under UV–LED irradiation and (**b**) change in the pH during the degradation.

In comparison, when ten surfaces were used, degradation efficiency was increased by 8%. Also, it was noticed that 5-TiO_2/Al surfaces were evenly mixed and distributed in a glass-jacketed beaker photocatalytic reactor. In contrast, when 10-TiO_2/Al surfaces were present in the photocatalytic reactor, some of the surfaces collided and overlapped, preventing the radiation from reaching and activating each surface evenly. Therefore, further tests were performed using 5-TiO_2/Al. The pH value was around 9.5 and did not change significantly during degradation (Figure 6b). At the beginning of the degradation process, the pH indicates the formation of more acidic intermediates, which were degraded during the photocatalytic process. At the end of the process, the pH was around 9.5.

From the economic point of view, as well as for practical applications, the reusability of photocatalysts is an underlying aspect to take into account for surface design [64]. Therefore, further investigations were directed toward examining the photostability and reusability of TiO_2/Al. $5-TiO_2/Al$, after the process of RB degradation, were collected, thoroughly washed twice with ultrapure water, and dried. Five successive photodegradation experiments were conducted while other experimental conditions were kept unchanged. Figure 7 shows five consecutive photodegradation treatments. The degradation efficiency was the same during the first three runs. There was a decrease in photocatalytic efficiency by 4% in the fourth run and 11% in the fifth run compared to the first use of $5-TO_2/Al$ surfaces. These findings point out that the dyes are very persistent contaminants, and there are not so many possible ways for their removal from the environment. $5-TiO_2/Al$ surfaces represent promising material due to their physical characteristics and easy removal of the foil from the dye solution. Also, they can be reused three times with the same efficiency.
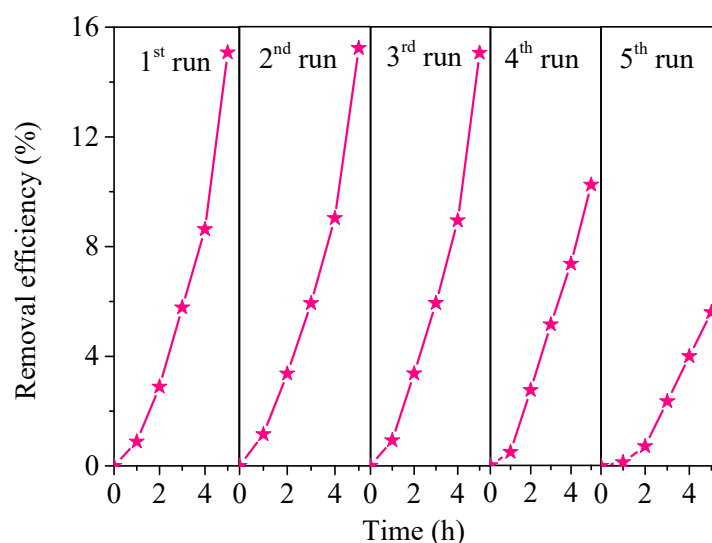

Figure 7. RB removal efficiency in the presence of reused $5-TiO_2/Al$ surfaces in five runs under UV–LED irradiation.

3.3. Influence of Different Irradiation Types

Since dyes are present in natural water bodies in the environment [65], wherein solar radiation is also present, further experiments were directed towards the use of SS irradiation, besides UV–LED irradiation. The efficiency of direct photolysis is dependent on the ability of the target dyes to absorb the emitted light and on the relevant quantum yields [66]. Therefore, direct photolysis of RB using SS and UV–LED irradiation was performed at a natural pH (9.5). Figure 8 shows direct photolysis and photocatalytic degradation of RB using $5-TiO_2/Al$. As can be seen, direct photolysis of RB was ineffective under SS and UV–LED irradiation, once again confirming the high stability of RB dye and its persistence in the environment. The degradation of RB using $5-TiO_2/Al$ under SS radiation was lower compared to degradation under UV–LED radiation. With the use of SS radiation, it was 5%, while with the use of UV–LED radiation, it was 16%. Keeping these results in mind, further degradation of dyes with synthesized $5-TiO_2/Al$ surfaces was performed using UV–LED radiation. Currently, UV–LED lamps are widely used, and they are much cheaper and more environmentally friendly.
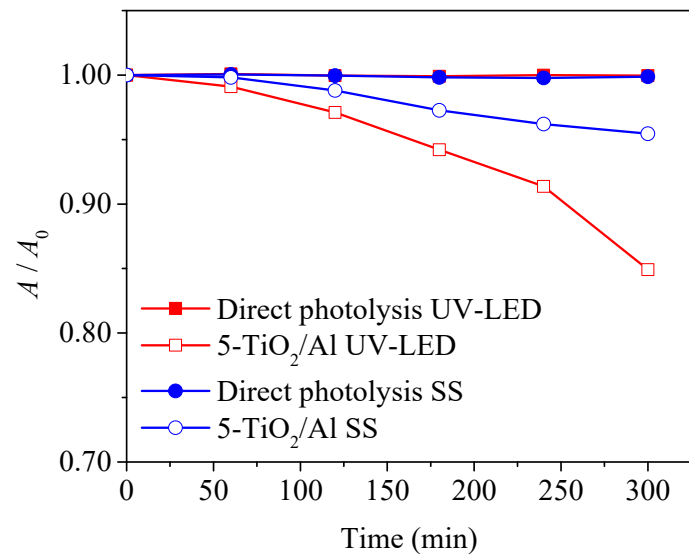
Figure 8. Direct photolysis and photocatalytic degradation of RB using 5-TiO$_2$/Al surfaces under SS and UV–LED irradiation.

3.4. Photodegradation of Various Dyes

To investigate the possibility of using synthesized 5-TiO$_2$/Al surfaces for the removal of different dyes, RB, MB, and MO degradation were examined. In order to examine the efficiency of synthesized 5-TiO$_2$/Al surfaces in the photodegradation of selected dyes, first, their direct photolysis was examined (Figure 9a). These three dyes showed stability during direct photolysis. pH value was 9.5 for RB, 9.7 for MO, and 10.0 for MB and did not change significantly during degradation (Figure 9b).
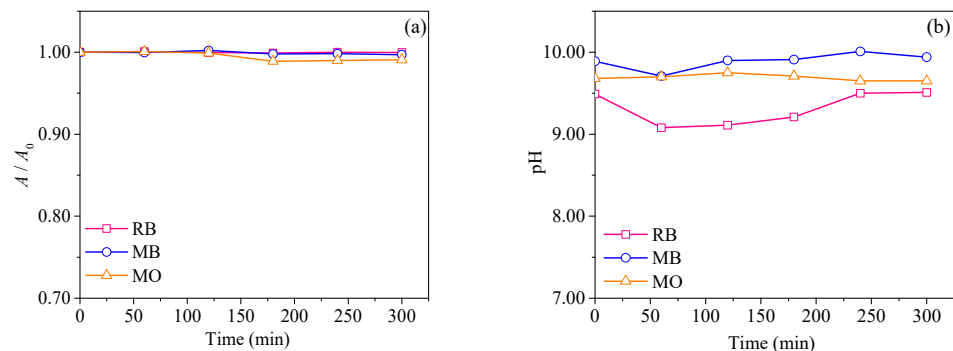

Figure 9. (**a**) Direct photolysis of different dyes under UV–LED irradiation and (**b**) change in the pH during the degradation.

Further, 5-TiO$_2$/Al surfaces were used for photodegradation of RB, MB, and MO under UV–LED irradiation. Degradation efficiency for MB was 10%, for RB 16%, and for MO 25% after 300 min of irradiation (Figure 10a). Different photodegradation efficiencies of dyes depend on their absorption maximum, structure, charge, and the number of condensed systems they contain. Namely, MO absorbs at 460 nm, and UV–LED lamp emission spectra give intensity at these wavelengths (Figures 1 and 2). RB absorbs at 560 nm, while MB absorbs at 660 nm (Figure 1), which explains their lower degradation efficiency. Interaction for cationic dyes (such as RB and MB) results from the repulsive electrostatic power between the positively charged surface of dyes and the catalyst. On the other hand, in the case of anionic dyes (such as MO), their negative surface charge increases the interaction and vice versa, depending on the charge of the catalyst surface. Since TiO$_2$ was responsible for the formation of reactive species (•OH radicals), which contributed to the degradation of the dyes, it is essential to discuss its surface charge in the dye solution. When the pH is

above 6.1 (herein it was above 9.5), the surface of TiO_2 is negatively charged. Cationic dyes, RB and MB, were positively charged in the solution, which can be the consequence of an attractive electrostatic force between the positively charged surface of the dyes and the negatively charged catalyst surface. However, the RB and MB were not adsorbed on the TiO_2/Al surfaces, but this may be the consequence of their lower degradation efficiency. On the other hand, in the case of anionic dye, MO, there is a repulsive electrostatic power between the negatively charged surface of MO and the negatively charged surface of the catalyst. Thus, adsorption is absent, and therefore, the efficiency of MO degradation was the highest. To sum up, none of the examined dyes were adsorbed on the TiO_2/Al surfaces. MO is an anionic dye, which is characterized by the presence of the NH group, which easily interacts with $^{\bullet}$OH radicals, therefore explaining the higher photodegradation of MO. Based on dye structure, MO does not have condensed systems, unlike the RB and MB, which once again explains its higher degradation. RB and MB have three condensed rings, which caused their slower degradation compared to the MO.
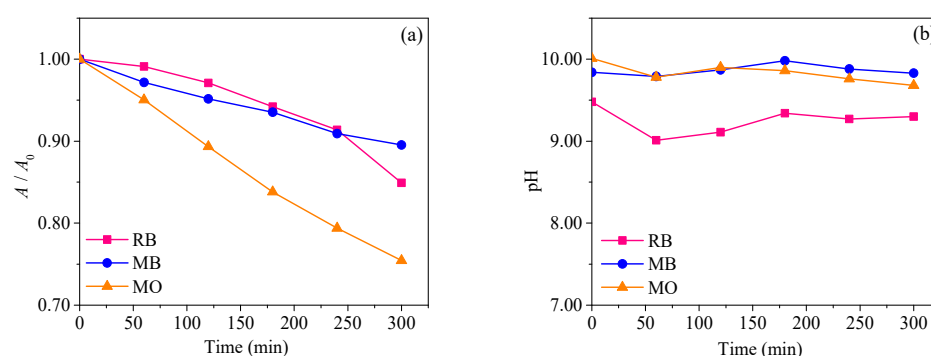

Figure 10. (**a**) The photocatalytic efficiency of 5-TiO_2/Al surfaces under UV–LED irradiation on different dyes and (**b**) the change in the pH during the degradation.

The pH value was around 9.5 for RB and 9.9 for MB and did not change significantly during degradation (Figure 10b). In the case of MO, pH was 10.0, and it decreased to 9.7, indicating the formation of acid intermediates during the degradation process.

3.5. Computational Study

The environmental fate of dyes is a highly complex process involving numerous parameters, making it challenging to understand the molecular-level interactions. Nevertheless, in the final section of this study, we employed modern computational methods to investigate the interaction between Al and TiO_2 and the interaction between dye molecules and a combined $AlTiO_2$ nanoparticle.

In the first part of the computational study, we focused on evaluating the binding between Al and TiO_2 nanoparticles. Experimental results from SEM/EDS clearly demonstrated the successful deposition of spherical TiO_2 nanoparticles on the aluminum matrix, which inspired us to study the interaction between Al and TiO_2 nanoparticles. This interaction serves as a model for the nanoparticle that interacts with the dye molecules. The initial step involved the geometric optimization of Al and TiO_2 nanoparticles. The starting atomic coordinates for the Al nanoparticle were generated using the nanoparticle builder of SMSS, while the initial atomic coordinates for the TiO_2 nanoparticle were taken from a reference that reported the ground state geometries of various TiO_2 clusters [51]. The TiO_2 cluster used in our study consisted of five TiO_2 units; hence, we refer to it as the TiO_2-5 cluster. The optimized geometries of the Al nanoparticle, the TiO_2-5 cluster, and their complex are presented in Figure 11.
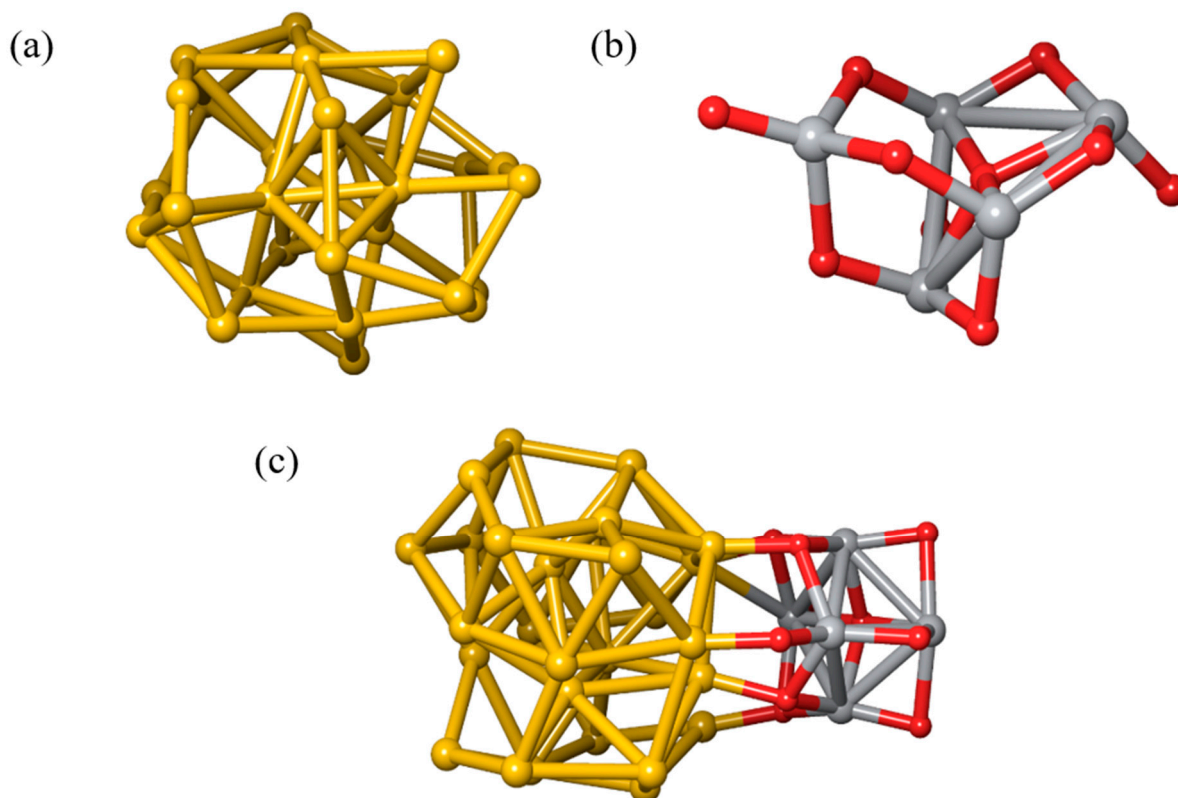
Figure 11. Optimized geometries of (**a**) Al nanoparticle, (**b**) TiO_2-5 nanoparticle, and (**c**) their complex, AlTiO_2. Yellow spheres represent Al nanoparticles, gray spheres represent titanium, and red spheres represent oxygen.

As illustrated in Figure 11, the geometric optimization of the complex consisting of Al and TiO_2-5 nanoparticles led to the formation of a single, cohesive nanoparticle, indicating a strong interaction between Al and TiO_2. This result aligns well with experimental findings, further supporting the hypothesis of the successful deposition of TiO_2 on the Al matrix. Additionally, recalculating the energies of the optimized structures at the ωB97X-3c level of theory yielded a binding energy of −147.66 kcal/mol (−6.40 eV), which is consistent with the experimental data. Thus, our computational results corroborate the experimental evidence of TiO_2 deposition on the Al.

Subsequently, the $AlTiO_2$ nanoparticle was employed as a model substrate for interacting with dye molecules. To explore these interactions, dye molecules were positioned above the $AlTiO_2$ nanoparticle, and geometric optimizations were performed at the PBE-D3/def2-SV(P) level of theory, followed by recalculations at the ωB97X-3c level to determine binding energies. The optimized geometries of the complexes are presented in Figure 12, and the corresponding binding energies are summarized in Table 2.

As evident from Figure 12, strong interactions occur between the $AlTiO_2$ nanoparticle and each dye molecule. Moreover, the differences in binding energies are significant, ranging from −44.26 kcal/mol to −106.98 kcal/mol. The lowest binding energy was calculated for the adsorption of RB, with a value of −44.26 kcal/mol. In contrast, the strongest binding energy was observed for the adsorption of MO dye, with a value of −106.98 kcal/mol. The binding energy for MB adsorption, although significantly lower than that for MO, is still much stronger than the binding energy for RB.

These binding energy results are consistent with the observed trend in photocatalytic degradation of dyes under UV–LED irradiation. Specifically, the results presented in Figure 10 clearly show that the degradation of MO is the fastest, significantly outpacing the degradation of MB and RB. The exceptionally strong binding of MO to the $AlTiO_2$ nanoparticle can be attributed to its planar structure, which allows for extensive π-π stack-

ing interactions with the surface, as well as the potential for multiple points of interaction, including hydrogen bonding and electrostatic interactions. The planar geometry of MO facilitates optimal surface contact, maximizing the interaction with the nanoparticle and leading to a more stable complex. This enhanced interaction likely plays a crucial role in the efficient removal of MO in the photocatalytic system proposed in this work.
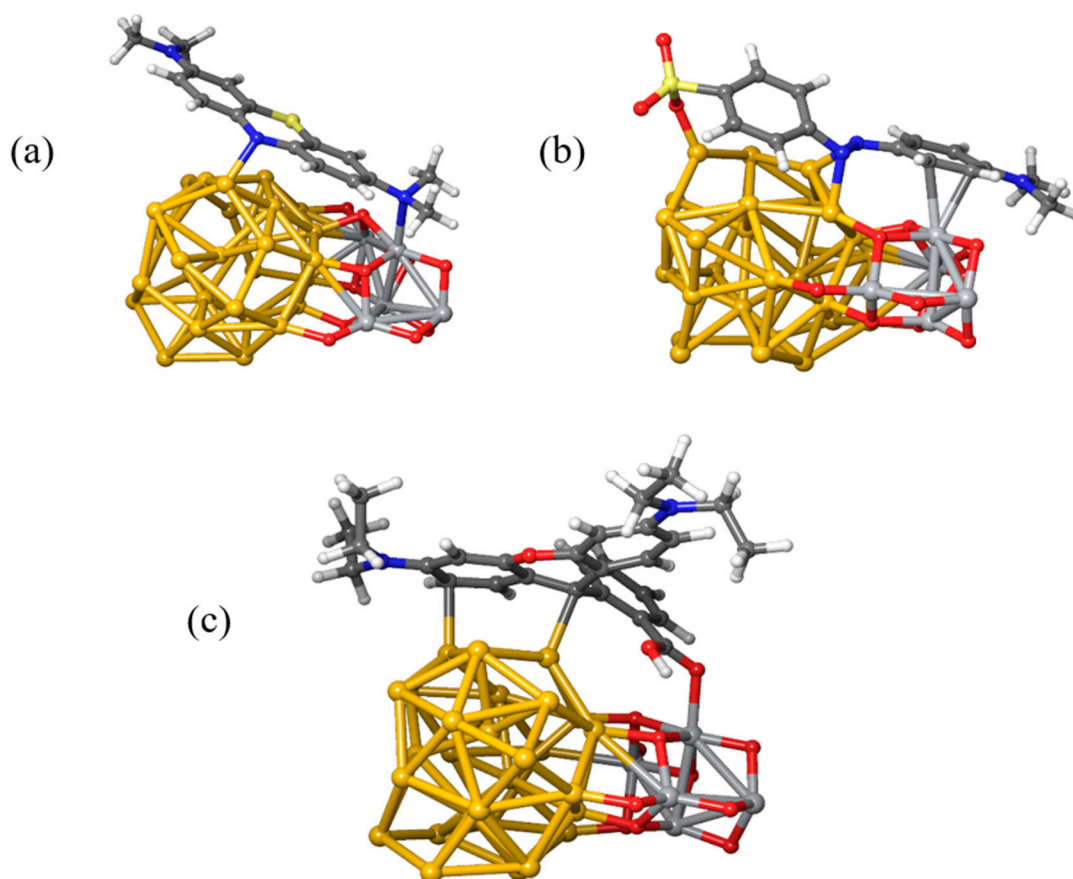

Figure 12. Optimized complexes of $AlTiO_2$ nanoparticle and studied dye molecules (**a**) $AlTiO_2$ + MB, (**b**) $AlTiO_2$ + MO, and (**c**) $AlTiO_2$ + RB. Yellow spheres represent Al nanoparticles, gray spheres represent titanium, and red spheres represent oxygen. In MB, MO, and RB molecules dark gray spheres represent carbon, white spheres represent hydrogen, red spheres represent oxygen, blue spheres represent nitrogen, and yellow spheres represent sulfur.

Table 2. Binding energies between $AlTiO_2$ nanoparticles and studied dyes.

Complex	E_b[kcal/mol]	E_b[eV]
$AlTiO_2$ + MB	−91.81	−3.98
$AlTiO_2$ + MO	−106.98	−4.64
$AlTiO_2$ + RB	−44.26	−1.92

4. Conclusions

In this study, we produced TiO_2-coated aluminum (TiO_2/Al) photoactive surfaces using eco-friendly and cost-effective methods. The spray method was employed to deposit TiO_2 layer films onto the foil surfaces. Scanning electron microscopy (SEM) and energy-dispersive X-ray spectroscopy (EDS) were used to analyze the morphology of TiO_2/Al surfaces both before and after photocatalytic treatment. Obtained results revealed spherical particles of TiO_2 and tunnel morphology of Al foil. Also, SEM micrographs revealed that spherical particles of TiO_2 were well-deposited on the foil. TiO_2 particles were organized on Al foil in such a way that there was an interparticle space of similar dimensions. This

enables dye molecules to be in contact with TiO_2 as well as with Al during the degradation process. From SEM micrographs, it seems that the TiO_2/Al surfaces of the composite are relatively inhomogeneous. The results support the idea that TiO_2/Al surfaces are a promising solution for water purification treatment owing to their activity, simplicity, and low processing cost.

Photocatalytic properties of the modified surfaces were evaluated through the photodegradation of RB in the presence of SS and UV–LED irradiation. The optimal number of TiO_2/Al coatings for RB photodegradation was five, wherein the most optimal degradation was achieved. When using 5-TiO_2/Al surfaces, the degradation efficiency of RB was 16%, while its mineralization was 5%. TiO_2/Al surfaces showed the possibility of reusing through five successive runs of RB degradation. TiO_2/Al could be used for the degradation of RB with the same efficiency three times. Higher degradation of RB was achieved using UV–LED irradiation, compared to SS irradiation. Namely, UV–LED lamps are widely used, and they are much cheaper. Also, the synthesized surfaces were tested for degradation of MB and MO, with the highest degradation observed for MO. Namely, MO absorbs at 460 nm, and UV–LED lamp emission spectra give intensity at these wavelengths, explaining its higher reactivity compared to RB (λ_{max} 560 nm) and MB (λ_{max} 660 nm). Also, MO represents an anionic dye, which is characterized by the presence of the NH group, which easily interacts with $^\bullet$OH radicals. MO does not have condensed systems, unlike RB and MB, which go in favor of its higher degradation. The repulsive electrostatic power between MO and catalyst contributed to the absence of adsorption and, therefore, to the highest efficiency of MO degradation. The computational study of interactions between dye molecules and the combined nanoparticle revealed that the binding was strongest in the case of MO dye adsorption. The binding energy for MO had a value of -106.98 kcal/mol. This finding closely aligns with the observed experimental results, which showed the most efficient degradation of MO under UV–LED irradiation.

References

1. Uddin, F. Environmental Hazard in Textile Dyeing Wastewater from Local Textile Industry. *Cellulose* **2021**, *28*, 10715–10739. [CrossRef]
2. Khattab, T.A.; Abdelrahman, M.S.; Rehan, M. Textile Dyeing Industry: Environmental Impacts and Remediation. *Environ. Sci. Pollut. Res.* **2020**, *27*, 3803–3818. [CrossRef] [PubMed]
3. Adegoke, K.A.; Bello, O.S. Dye Sequestration Using Agricultural Wastes as Adsorbents. *Water Resour. Ind.* **2015**, *12*, 8–24. [CrossRef]

4. Khan, W.U.; Ahmed, S.; Dhoble, Y.; Madhav, S. A Critical Review of Hazardous Waste Generation from Textile Industries and Associated Ecological Impacts. *J. Indian Chem. Soc.* **2023**, *100*, 100829. [CrossRef]

5. Alsukaibi, A.K.D. Various Approaches for the Detoxification of Toxic Dyes in Wastewater. *Processes* **2022**, *10*, 1968. [CrossRef]

6. Ardila-Leal, L.D.; Poutou-Piñales, R.A.; Pedroza-Rodríguez, A.M.; Quevedo-Hidalgo, B.E. A Brief History of Colour, the Environmental Impact of Synthetic Dyes and Removal by Using Laccases. *Molecules* **2021**, *26*, 3813. [CrossRef]

7. Islam, T.; Repon, M.R.; Islam, T.; Sarwar, Z.; Rahman, M.M. Impact of Textile Dyes on Health and Ecosystem: A Review of Structure, Causes, and Potential Solutions. *Environ. Sci. Pollut. Res.* **2022**, *30*, 9207–9242. [CrossRef]

8. Sharma, J.; Sharma, S.; Soni, V. Classification and Impact of Synthetic Textile Dyes on Aquatic Flora: A Review. *Reg. Stud. Mar. Sci.* **2021**, *45*, 101802. [CrossRef]

9. Pereira, L.; Alves, M. Dyes—Environmental Impact and Remediation. In *Environmental Protection Strategies for Sustainable Development*; Malik, A., Grohmann, E., Eds.; Springer: Dordrecht, The Netherlands, 2012; pp. 111–162, ISBN 978-94-007-1590-5.

10. Talaiekhozani, A.; Rezania, S. Application of Photosynthetic Bacteria for Removal of Heavy Metals, Macro-Pollutants and Dye from Wastewater: A Review. *J. Water Process Eng.* **2017**, *19*, 312–321. [CrossRef]

11. Monisha, B.; Sridharan, R.; Kumar, P.S.; Rangasamy, G.; Krishnaswamy, V.G.; Subhashree, S. Sensing of Azo Toxic Dyes Using Nanomaterials and Its Health Effects—A Review. *Chemosphere* **2023**, *313*, 137614. [CrossRef]

12. Gičević, A.; Hindija, L.; Karačić, A. Toxicity of Azo Dyes in Pharmaceutical Industry. In *CMBEBIH 2019*; Badnjevic, A., Škrbić, R., Gurbeta Pokvić, L., Eds.; IFMBE Proceedings; Springer International Publishing: Cham, Switzerland, 2020; Volume 73, pp. 581–587, ISBN 978-3-030-17970-0.

13. Ou, W.; Xu, Y.; Zhou, H.; Su, C. Harnessing Photoexcited Redox Centers of Semiconductor Photocatalysts for Advanced Synthetic Chemistry. *Sol. RRL* **2021**, *5*, 2000444. [CrossRef]

14. Zhang, D.; Li, G.; Yu, J.C. Inorganic Materials for Photocatalytic Water Disinfection. *J. Mater. Chem.* **2010**, *20*, 4529. [CrossRef]

15. Serpone, N.; Emeline, A.V. Semiconductor Photocatalysis—Past, Present, and Future Outlook. *J. Phys. Chem. Lett.* **2012**, *3*, 673–677. [CrossRef]

16. Nam, Y.; Lim, J.H.; Ko, K.C.; Lee, J.Y. Photocatalytic Activity of TiO_2 Nanoparticles: A Theoretical Aspect. *J. Mater. Chem. A* **2019**, *7*, 13833–13859. [CrossRef]

17. Bhatia, S.; Verma, N. Photocatalytic Activity of ZnO Nanoparticles with Optimization of Defects. *Mater. Res. Bull.* **2017**, *95*, 468–476. [CrossRef]

18. Fu, H.; Zhang, L.; Yao, W.; Zhu, Y. Photocatalytic Properties of Nanosized Bi2WO6 Catalysts Synthesized via a Hydrothermal Process. *Appl. Catal. B Environ.* **2006**, *66*, 100–110. [CrossRef]

19. Carcel, R.A.; Andronic, L.; Duta, A. Photocatalytic Activity and Stability of TiO_2 and WO_3 Thin Films. *Mater. Charact.* **2012**, *70*, 68–73. [CrossRef]

20. Luo, Z.; Meng, L.; How, Z.T.; Chelme-Ayala, P.; Yang, L.; Benally, C.; Gamal El-Din, M. Treatment of Oil Sands Process Water by the Ferric Citrate under Visible Light Irradiation. *Chem. Eng. J.* **2022**, *429*, 132419. [CrossRef]

21. Armaković, S.J.; Savanović, M.M.; Armaković, S. Titanium Dioxide as the Most Used Photocatalyst for Water Purification: An Overview. *Catalysts* **2022**, *13*, 26. [CrossRef]

22. Jeon, J.; Kweon, D.H.; Jang, B.J.; Ju, M.J.; Baek, J. Enhancing the Photocatalytic Activity of TiO_2 Catalysts. *Adv. Sustain. Syst.* **2020**, *4*, 2000197. [CrossRef]

23. Basavarajappa, P.S.; Patil, S.B.; Ganganagappa, N.; Reddy, K.R.; Raghu, A.V.; Reddy, C.V. Recent Progress in Metal-Doped TiO_2, Non-Metal Doped/Codoped TiO_2 and TiO_2 Nanostructured Hybrids for Enhanced Photocatalysis. *Int. J. Hydrogen Energy* **2020**, *45*, 7764–7778. [CrossRef]

24. Ma, T.; Inoue, K.; Noma, H.; Yao, K.; Abe, E. Effect of Functional Group on Photochemical Properties and Photosensitization of TiO_2 Electrode Sensitized by Porphyrin Derivatives. *J. Photochem. Photobiol. Chem.* **2002**, *152*, 207–212. [CrossRef]

25. Armaković, S.J.; Armaković, S.; Savanović, M.M. Photocatalytic Application of Polymers in Removing Pharmaceuticals from Water: A Comprehensive Review. *Catalysts* **2024**, *14*, 447. [CrossRef]

26. Yan, B.; Lv, X.; Shao, Y.; Zhang, H.; Zhang, H.; Zhu, J. Fabrication of Nano TiO_2-Polymer Encapsulated Fluorescent Pigments for Weatherability Improvement of Powder Coating. *Coatings* **2022**, *12*, 315. [CrossRef]

27. Fan, S.-Q.; Yang, G.-J.; Li, C.-J.; Liu, G.-J.; Li, C.-X.; Zhang, L.-Z. Characterization of Microstructure of Nano-TiO_2 Coating Deposited by Vacuum Cold Spraying. *J. Therm. Spray Technol.* **2006**, *15*, 513–517. [CrossRef]

28. Chen, D.; Cheng, Y.; Zhou, N.; Chen, P.; Wang, Y.; Li, K.; Huo, S.; Cheng, P.; Peng, P.; Zhang, R.; et al. Photocatalytic Degradation of Organic Pollutants Using TiO_2-Based Photocatalysts: A Review. *J. Clean. Prod.* **2020**, *268*, 121725. [CrossRef]

29. Dell'Edera, M.; Lo Porto, C.; De Pasquale, I.; Petronella, F.; Curri, M.L.; Agostiano, A.; Comparelli, R. Photocatalytic TiO_2-Based Coatings for Environmental Applications. *Catal. Today* **2021**, *380*, 62–83. [CrossRef]

30. Tomić, J.; Malinović, N. Titanium Dioxide Photocatalyst: Present Situation and Future Approaches. *AIDASCO Rev.* **2023**, *1*, 26–30. [CrossRef]

31. Tao, P.; Li, Y.; Rungta, A.; Viswanath, A.; Gao, J.; Benicewicz, B.C.; Siegel, R.W.; Schadler, L.S. TiO_2 Nanocomposites with High Refractive Index and Transparency. *J. Mater. Chem.* **2011**, *21*, 18623. [CrossRef]

32. Bennani, J.; Dillert, R.; Gesing, T.M.; Bahnemann, D. Physical Properties, Stability, and Photocatalytic Activity of Transparent TiO_2/SiO_2 Films. *Sep. Purif. Technol.* **2009**, *67*, 173–179. [CrossRef]

33. Obregón, S.; Rodríguez-González, V. Photocatalytic TiO₂ Thin Films and Coatings Prepared by Sol–Gel Processing: A Brief Review. *J. Sol-Gel Sci. Technol.* **2022**, *102*, 125–141. [CrossRef]

34. Gloria, D.C.S.; Brito, C.H.V.; Mendonça, T.A.P.; Brazil, T.R.; Domingues, R.A.; Vieira, N.C.S.; Santos, E.B.; Gonçalves, M. Preparation of TiO₂/Activated Carbon Nanomaterials with Enhanced Photocatalytic Activity in Paracetamol Degradation. *Mater. Chem. Phys.* **2023**, *305*, 127947. [CrossRef]

35. Ma, R.; Zhao, S.; Jiang, X.; Qi, Y.; Zhao, T.; Liu, Z.; Han, C.; Shen, Y. Modification and Regulation of Acid-Activated Kaolinite with TiO₂ Nanoparticles and Their Enhanced Photocatalytic Activity to Sodium Ethyl Xanthate. *Environ. Technol. Rev.* **2023**, *12*, 272–285. [CrossRef]

36. Al-Mamun, M.R.; Kader, S.; Islam, M.S.; Khan, M.Z.H. Photocatalytic Activity Improvement and Application of UV-TiO₂ Photocatalysis in Textile Wastewater Treatment: A Review. *J. Environ. Chem. Eng.* **2019**, *7*, 103248. [CrossRef]

37. Ehlert, S.; Stahn, M.; Spicher, S.; Grimme, S. Robust and Efficient Implicit Solvation Model for Fast Semiempirical Methods. *J. Chem. Theory Comput.* **2021**, *17*, 4250–4261. [CrossRef]

38. Bannwarth, C.; Caldeweyher, E.; Ehlert, S.; Hansen, A.; Pracht, P.; Seibert, J.; Spicher, S.; Grimme, S. Extended Tight-Binding Quantum Chemistry Methods. *WIREs Comput. Mol. Sci.* **2021**, *11*, e1493. [CrossRef]

39. Bannwarth, C.; Ehlert, S.; Grimme, S. GFN2-xTB—An Accurate and Broadly Parametrized Self-Consistent Tight-Binding Quantum Chemical Method with Multipole Electrostatics and Density-Dependent Dispersion Contributions. *J. Chem. Theory Comput.* **2019**, *15*, 1652–1671. [CrossRef]

40. Pracht, P.; Caldeweyher, E.; Ehlert, S.; Grimme, S. A Robust Non-Self-Consistent Tight-Binding Quantum Chemistry Method for Large Molecules. *ChemRxiv* **2019**. [CrossRef]

41. Grimme, S.; Bannwarth, C.; Shushkov, P. A Robust and Accurate Tight-Binding Quantum Chemical Method for Structures, Vibrational Frequencies, and Noncovalent Interactions of Large Molecular Systems Parametrized for All Spd-Block Elements (Z = 1–86). *J. Chem. Theory Comput.* **2017**, *13*, 1989–2009. [CrossRef]

42. Perdew, J.P.; Burke, K.; Ernzerhof, M. Generalized Gradient Approximation Made Simple. *Phys. Rev. Lett.* **1996**, *77*, 3865–3868; Erratum in *Phys. Rev. Lett.* **1997**, *78*, 1396. [CrossRef]

43. Smith, D.G.A.; Burns, L.A.; Patkowski, K.; Sherrill, C.D. Revised Damping Parameters for the D3 Dispersion Correction to Density Functional Theory. *J. Phys. Chem. Lett.* **2016**, *7*, 2197–2203. [CrossRef] [PubMed]

44. Grimme, S.; Ehrlich, S.; Goerigk, L. Effect of the Damping Function in Dispersion Corrected Density Functional Theory. *J. Comput. Chem.* **2011**, *32*, 1456–1465. [CrossRef]

45. Grimme, S.; Antony, J.; Ehrlich, S.; Krieg, H. A Consistent and Accurate Ab Initio Parametrization of Density Functional Dispersion Correction (DFT-D) for the 94 Elements H-Pu. *J. Chem. Phys.* **2010**, *132*, 154104. [CrossRef] [PubMed]

46. Müller, M.; Hansen, A.; Grimme, S. ωB97X-3c: A Composite Range-Separated Hybrid DFT Method with a Molecule-Optimized Polarized Valence Double-ζ Basis Set. *J. Chem. Phys.* **2023**, *158*, 014103. [CrossRef] [PubMed]

47. Cao, Y.; Halls, M.D.; Vadicherla, T.R.; Friesner, R.A. Pseudospectral Implementations of Long-Range Corrected Density Functional Theory. *J. Comput. Chem.* **2021**, *42*, 2089–2102. [CrossRef] [PubMed]

48. Jacobson, L.D.; Bochevarov, A.D.; Watson, M.A.; Hughes, T.F.; Rinaldo, D.; Ehrlich, S.; Steinbrecher, T.B.; Vaitheeswaran, S.; Philipp, D.M.; Halls, M.D. Automated Transition State Search and Its Application to Diverse Types of Organic Reactions. *J. Chem. Theory Comput.* **2017**, *13*, 5780–5797. [CrossRef]

49. Cao, Y.; Hughes, T.; Giesen, D.; Halls, M.D.; Goldberg, A.; Vadicherla, T.R.; Sastry, M.; Patel, B.; Sherman, W.; Weisman, A.L.; et al. Highly Efficient Implementation of Pseudospectral Time-Dependent Density-Functional Theory for the Calculation of Excitation Energies of Large Molecules. *J. Comput. Chem.* **2016**, *37*, 1425–1441. [CrossRef]

50. Bochevarov, A.D.; Harder, E.; Hughes, T.F.; Greenwood, J.R.; Braden, D.A.; Philipp, D.M.; Rinaldo, D.; Halls, M.D.; Zhang, J.; Friesner, R.A. Jaguar: A High-Performance Quantum Chemistry Software Program with Strengths in Life and Materials Sciences. *Int. J. Quantum Chem.* **2013**, *113*, 2110–2142. [CrossRef]

51. Berardo, E.; Hu, H.-S.; van Dam, H.J.J.; Shevlin, S.A.; Woodley, S.M.; Kowalski, K.; Zwijnenburg, M.A. Describing Excited State Relaxation and Localization in TiO₂ Nanoparticles Using TD-DFT. *J. Chem. Theory Comput.* **2014**, *10*, 5538–5548. [CrossRef]

52. Helmich-Paris, B.; de Souza, B.; Neese, F.; Izsák, R. An Improved Chain of Spheres for Exchange Algorithm. *J. Chem. Phys.* **2021**, *155*, 104109. [CrossRef]

53. Neese, F. An Improvement of the Resolution of the Identity Approximation for the Formation of the Coulomb Matrix. *J. Comput. Chem.* **2003**, *24*, 1740–1747. [CrossRef] [PubMed]

54. Neese, F.; Wennmohs, F.; Hansen, A.; Becker, U. Efficient, Approximate and Parallel Hartree–Fock and Hybrid DFT Calculations. A 'Chain-of-Spheres' Algorithm for the Hartree–Fock Exchange. *Chem. Phys.* **2009**, *356*, 98–109. [CrossRef]

55. Neese, F.; Wennmohs, F.; Becker, U.; Riplinger, C. The ORCA Quantum Chemistry Program Package. *J. Chem. Phys.* **2020**, *152*, 224108. [CrossRef] [PubMed]

56. Neese, F. The SHARK Integral Generation and Digestion System. *J. Comput. Chem.* **2023**, *44*, 381–396. [CrossRef]

57. Neese, F. Software Update: The ORCA Program System, Version 4.0. *WIRES Comput. Mol. Sci.* **2018**, *8*, e1327. [CrossRef]

58. Neese, F. The ORCA Program System. *WIRES Comput. Mol. Sci.* **2012**, *2*, 73–78. [CrossRef]

59. Neese, F. Approximate Second-Order SCF Convergence for Spin Unrestricted Wavefunctions. *Chem. Phys. Lett.* **2000**, *325*, 93–98. [CrossRef]

60. Neese, F. Software Update: The ORCA Program System, Version 5.0. *WIRES Comput. Mol. Sci.* **2022**, *12*, e1606. [CrossRef]

61. Armaković, S.; Armaković, S.J. Atomistica.Online—Web Application for Generating Input Files for ORCA Molecular Modelling Package Made with the Anvil Platform. *Mol. Simul.* **2023**, *49*, 117–123. [CrossRef]

62. Armaković, S.; Armaković, S.J. Online and Desktop Graphical User Interfaces for Xtb Programme from Atomistica.Online Platform. *Mol. Simul.* **2024**, *50*, 560–570. [CrossRef]

63. Henning, S.; Adhikari, R. Scanning Electron Microscopy, ESEM, and X-ray Microanalysis. In *Microscopy Methods in Nanomaterials Characterization*; Elsevier: Amsterdam, The Netherlands, 2017; pp. 1–30, ISBN 978-0-323-46141-2.

64. Frederichi, D.; Scaliante, M.H.N.O.; Bergamasco, R. Structured Photocatalytic Systems: Photocatalytic Coatings on Low-Cost Structures for Treatment of Water Contaminated with Micropollutants—A Short Review. *Environ. Sci. Pollut. Res.* **2021**, *28*, 23610–23633. [CrossRef] [PubMed]

65. Batchu, S.R.; Panditi, V.R.; O'Shea, K.E.; Gardinali, P.R. Photodegradation of Antibiotics under Simulated Solar Radiation: Implications for Their Environmental Fate. *Sci. Total Environ.* **2014**, *470–471*, 299–310. [CrossRef] [PubMed]

66. Chowdhury, P.; Sarathy, S.R.; Das, S.; Li, J.; Ray, A.K.; Ray, M.B. Direct UV Photolysis of Pharmaceutical Compounds: Determination of pH-Dependent Quantum Yield and Full-Scale Performance. *Chem. Eng. J.* **2020**, *380*, 122460. [CrossRef]